Disclosing the response of the surface electronic structure in SrTiO₃ (001) to strain Ⓕ

Eduardo Bonini Guedes,[1] Ⓘ Tobias Willemoes Jensen,[2] Ⓘ Muntaser Naamneh,[1,3] Ⓘ Alla Chikina,[1] Ⓘ
Ramus T. Dahm,[2] Ⓘ Shinhee Yun,[2] Ⓘ Francesco M. Chiabrera,[2] Ⓘ Nicholas C. Plumb,[1] Ⓘ J. Hugo Dil,[1,4] Ⓘ
Ming Shi,[1] Dennis Valbjørn Christensen,[2] Ⓘ Walber Hugo Brito,[5] Ⓘ Nini Pryds,[2] Ⓘ and Milan Radović[1] Ⓘ

AFFILIATIONS

[1]Photon Science Division, Paul Scherrer Institut, CH-5232 Villigen, Switzerland
[2]Department of Energy Conversion and Storage, Technical University of Denmark, Fysikvej, 2800 Kgs. Lyngby, Denmark
[3]Department of Physics, Ben-Gurion University of the Negev, Beer-Sheva 84105, Israel
[4]Institut de Physique, École Polytechnique Fédérale de Lausanne, CH-1015 Lausanne, Switzerland
[5]Departamento de Física, Universidade Federal de Minas Gerais, C.P. 702, 30123-970 Belo Horizonte, Minas Gerais, Brazil

Note: This paper is a part of the Special Collection Honoring Dr. Scott Chambers' 70th Birthday and His Leadership in the Science and Technology of Oxide Thin Films.

ABSTRACT

Combining angle-resolved photoemission spectroscopy and density functional theory calculations, we addressed the surface electronic structure of bent SrTiO₃ (STO) (001) wafers. Using a custom-made device, we observe that the low-dimensional states that emerge at the STO (001) surface are robust to an external tensile strain of about 0.1%. Our results show that this value of strain is too small to sensibly alter the surface conduction band of STO, but, surprisingly, it is enough to shift the energy of the in-gap states. In order to access higher strain values of around 2%, standard for STO-based heterostructures, we performed density functional theory calculations of STO slabs under different strain configurations. The simulations predict that such levels of both compressive and tensile strain significantly alter the orbital splitting of the surface conduction band. Our study indicates that the strain generated in STO can tailor the electronic properties of its bare surface and of STO-based interfaces.

I. INTRODUCTION

Transition metal oxides (TMOs) exhibit a wide variety of exotic and very promising properties, such as high-temperature superconductivity,[1] colossal magnetoresistance,[2] wide-ranging magnetically ordered states,[3] metal-insulator transitions (MITs),[4] ferroelectricity,[5] and multiferroicity.[6] The interplay between the electronic and lattice degrees of freedom in the TMO compound, distinguished by a partially filled *d* orbital, opens a possibility to further tune the emerging physical properties. In addition, surfaces and interfaces present an additional playground[7] where physical properties can be altered mostly due to heteroepitaxy and defects. Indeed, it was demonstrated that external pressure and epitaxial strain affect the physical properties of TMO, such as MIT[8] or ferroelectricity.[9] For instance, by combining thin film growth and angle-resolved photoemission (ARPES), it was shown that epitaxial strain engineering affects the Fermi surface topology and many-body interactions in two-dimensional ruthenates.[10]

The low-dimensional electronic system (LDES) at the interface between SrTiO₃ (STO) and LaAlO₃ (LAO)[11] motivates extensive research to understand its origin and to develop methods for tuning physical parameters.[12] However, it is challenging to disentangle and study the impact of different effects (stain, charge transfer, polar discontinuity, defects, surface termination, etc.) on the physical properties at the usual LAO/STO interface individually. Favorably, the finding of the low-dimensional electronic state (LDES) on a surface of the STO wafer[13–15] grants us with an unadulterated playground for studying this marvel using very susceptible methods such as scanning tunneling spectroscopy (STM)[16] and angle-resolved photoemission spectroscopy (ARPES).[13–15,17]

A recent study reports that a relatively standard annealing temperature of 550 °C in an oxygen-rich atmosphere leads to a

Sr-rich surface,[18] consequently favoring the formation of 2DEG at the surface, similar to findings related to SrO-terminated STO films.[19] STO used as a substrate undergoes extreme annealing procedures during the film growth, which must also be considered. However, STO films grown on STO[20] or NdGaO$_3$ (110)[21] show a tendency to end with Sr-rich surfaces. One of the important features of the LDES is a relatively large splitting between d$_{xy}$ and d$_{xz}$/d$_{yz}$ bands,[15,18] suggesting that deviations from the cubic (or slightly tetragonal when at low temperatures) structure occurs at the surface region. The enhancement of the electron mobility of over 300% observed in La-doped STO films under uniaxial stress[22] confirmed that the strain could be effectively used for altering the STO bulk properties. Furthermore, it was shown by ARPES measurements that *in situ* strain modifies the electronic structure of doped bulk 2D ruthenates.[23] Hence, altering the surface crystal structure can presumably tune the electronic properties of the LDES at the STO surface.

In this work, combining ARPES with DFT simulations, we investigated the response of the STO (001) surface electronic structure to an externally applied structural perturbation by mechanically bending the crystal.

II. METHODS AND MATERIALS

Commercially available STO (001) wafers (SurfaceNET GmbH) were mounted on a custom-made device, referred to as a bender, as shown in Fig. 1. The screw pushes a cylindrical part of the bender that subsequently induces strain on the substrate, as shown schematically in Figs. 1(a) and 1(d). The cylinder displacement is controlled by turning a screw with a conical tip, which serves as a wedge. By rotating the screw, the cylinder's displacement forces the STO wafer to bend, thereby creating strains in the sample.[22] The actual profile of a bent 500 μm thick STO (5×10 mm^2) wafer was measured at different displacements with a Cyberscan Vantage optical profilometer. The resulting data, as shown in figure Fig. 1(b), are fitted to parabolas of the form $y = ax^2 + bx + c$, where $C = 2a$ is the maximum curvature. The profilometry data show that the STO wafer bends around its shorter symmetry axes. We have estimated a generated strain by multiplying curvatures (C) by half the thickness of the wafer $S = C \cdot t/2$.[22] The produced strain vs displacement is presented in Fig. 1(c). The error bars are the standard deviations of the calculated strain across all lines in a single profilometry measurement.

Using the COMSOL Multiphysics® software[24], we calculated a generated strain for the bent slab of 500 μm STO with the edges fixed. We have assumed that displacements in the middle of the wafer form a straight line. With this assumption, COMSOL Multiphysics® was used to simulate the bending of the wafer, mimicking the one that occurs using the cylinder in the bender. The simulations generated intuitively expected results: the bent STO wafer is expanded in the long direction, i.e., in the sample plane perpendicular to the cylinder axis, which we assign as x-direction, while it is compressed in the direction perpendicular to the sample surface, assigned as x-direction. In contrast, along with the cylinder axis, identified as the sample y-direction, the sample is negligibly affected compared to the previous two directions. The calculated strains in all three directions are plotted in Fig. 1(c), as a function of the displacements at the middle of the wafer, along with the strain estimated from the profilometry data. The 2D map of calculated strains for 30 μm displacement is shown in Figs. 1(e)–1(g).

The electronic band structures of two STO wafers strained with a progressive force have been investigated using ARPES at the SIS beamline of the Swiss Light Source. The same bender, previously characterized with profilometry measurements, was specially designed to serve also as a sample holder compatible with our ARPES setup. The bender device is designed based on a standard mushroom-like sample holder [see Fig. 1(d)] in such a way that the applied force can be adjusted *in situ* using a screwdriver installed on the wobble stick.

The experimental data were compared with the aid of DFT calculations performed within the Perdew–Burke–Ernzehof generalized gradient approximation (GGA-PBE),[25] using projector augmented-wave (PAW) potentials,[26] as implemented in the Vienna *Ab initio* Simulation Package (VASP).[27,28] In addition, we employed the DFT+U functional of Liechtenstein,[29] which takes into account the electronic interactions at a mean-field level by means of a partially screened Coulomb interaction $U = 5.0$ eV and $J = 0.64$ eV. The structural optimizations were done until the forces on each atom were less than 0.01 eV/Å. An energy cutoff of 500 eV was used for our plane-wave basis set. A k-mesh grid of $10 \times 10 \times 2$ was employed in the evaluation of the band structures.

III. RESULTS

The ARPES measurements were carried out on two differently treated 2 wt. % Nb-doped STO (001) wafers, both nominally TiO$_2$ terminated. In order to understand how natural adsorbents (arising from exposure to air) impact the 2DEG, the first sample was measured "as received" (without any additional treatment), serving as a reference to examine the bent STO crystal's electronic structure, and it is referred to as *nonannealed* (N-A). The second sample, referred as *annealed* (A), was annealed at 500 °C in 100 mbar of O$_2$ for 1 h to remove surface contamination and then *in situ* transferred to the ARPES instrument. The ARPES data were acquired at different bending levels, always with the synchrotron beam positioned at the center of the sample, mapping the electron structure of the conduction and the valence band at 20 K. The strain generated in STO samples was estimated as explained in the Methods section above.

At first exposure of the sample to synchrotron light of 85 eV, the ARPES spectrum shows no indication of states at the Fermi level (E$_F$). During the measurements, states with parabolic dispersion develop, showing the intensity increase and finally saturate. All the data shown in Figs. 2 and 3 were obtained at the saturated state.

The photo-induced 2DEG formed on the STO surface at this temperature exhibits a well-known band structure arising from the three orbitals with t$_{2g}$ symmetry in the conduction band. Figure 2 shows the ARPES data obtained with 85 eV, circularly polarized light. Panels (a)–(f) display the data of the N-A sample, while panels (g)–(l) show the band structure of the A sample. Panels (b), (e), (h), and (k) show band dispersion maps of samples without any applied force, while panels (c), (f), (i), and (l) show the equivalent data of samples with maximum applied force (just before sample breaks). The maximum strain was estimated to be 0.1%.
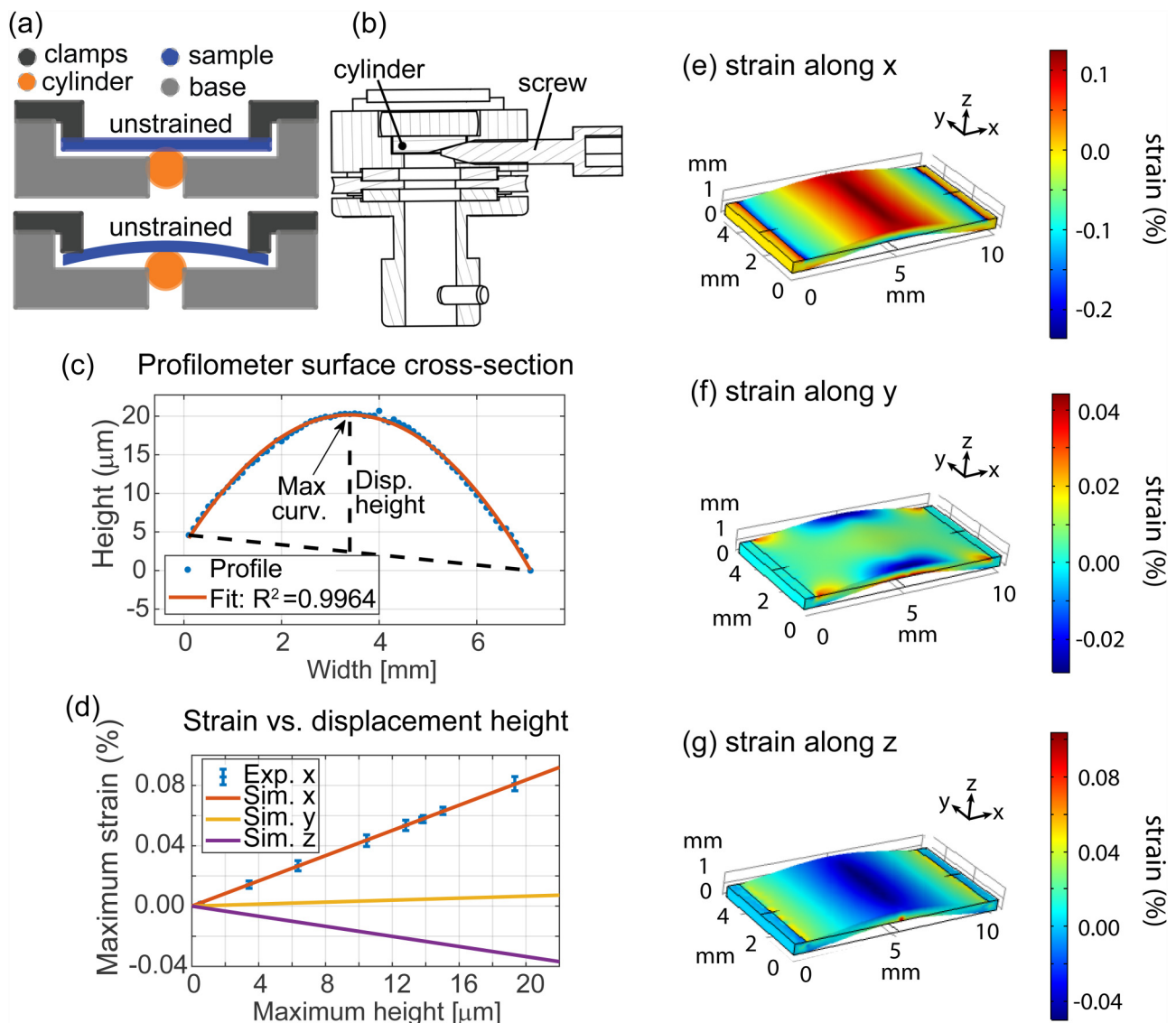
FIG. 1. (a) Schematic of the strain device, showing how a centered cylinder can force a sample to bend. (b) Cross section of a measured bend profile, fitted to a parabola, from which the curvature and strain can be calculated. (c) Experimental strain data along with the simulated strain in the center of the slabs shown in (e)–(g), as a function of displacement height. (d) Schematic of the strain device, where the cylinder from (a) is shown along with the screw which forces it up against the sample. (e)–(g) The x, y, and z strains, respectively, simulated in COMSOL Multiphysics®, at 30 μm deflection.

The used photon energy was chosen such that it is possible to measure the band structure that corresponds to the bulk Γ point, while C+ polarization enables to capture the contributions from all orbitals of the t_{2g} manifold.[15]

Matrix element effects, i.e., modulations of the spectral intensity caused by the dependence of the ARPES data on photon energy and experimental geometry,[30] are known to greatly impact the observation of the 2DEG on STO.[14,15,18] In particular, the bottom of the d_{yz} band and the outer d_{xy} band are easily seen around $\overline{\Gamma}_{00}$, while the bottom of the $d_{xy,xz}$ bands are very clear around $\overline{\Gamma}_{10}$.[15] Thus, the measurements were performed around both the $\overline{\Gamma}_{00}$ and $\overline{\Gamma}_{10}$ points, which allowed us to identify all the features in the spectra necessary for the reliable analysis of the data. The respective band dispersion maps in Fig. 2 were obtained along ΓX at $k_y = 0$, represented by the horizontal line in Fermi surface (FS) maps on Figs. 2(a), 2(d), 2(g), and 2(j).

The $d_{xz,yz}$ (out-of-plane) orbitals form heavy bands (along either k_x or k_y) with a mixed 2D/3D character, while a light band with 2D character arises from the in-plane d_{xy} orbital.[15] The d_{xy}-, d_{xz}-, and d_{yz}-derived bands remain degenerate for the N-A sample,
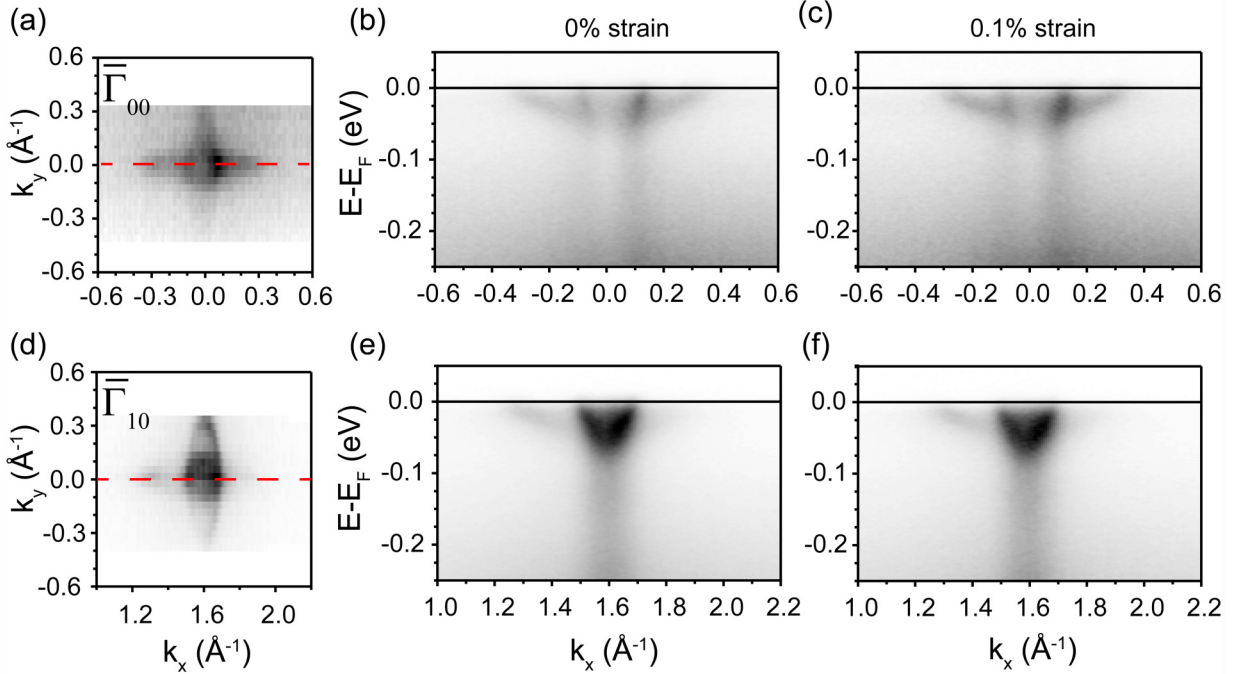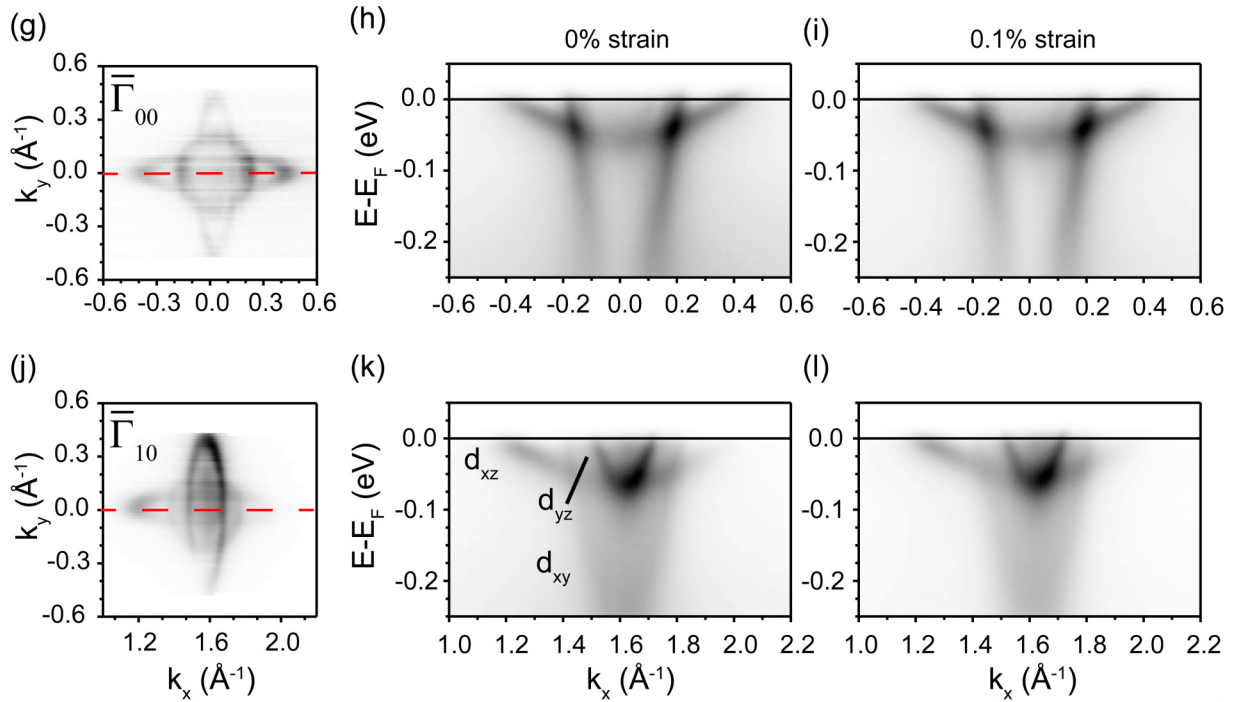
FIG. 2. ARPES data of the nonannealed (N-A) and annealed (A) STO (001) samples collected around the $\overline{\Gamma}_{00}$ and $\overline{\Gamma}_{01}$ points along the ΓX direction. Fermi surfaces (FSs) of N-A sample (a) and (d) and A sample (g) and (j). The conduction bands corresponding to the band dispersion map along the red line in the Fermi surfaces for both no strained, N-A sample (b) and (e), and A sample (h) and (k). The same maps for strained N-A (c) and (f) and A samples (i) and (l).

resembling the bulk conduction band, while, for the A sample, the bottom of the d_{xy} band shifts around 180 meV to lower binding energies. This increases the separation between the light and heavy bands, indicating a change in the surface structure.[18] The light band was previously observed to further split into lower and upper branches with opposite spin winding,[31] although the two branches are not well resolved using $h\nu = 85$ eV.[20] The very distinct band structure found in the N-A and A samples indicate that the adsorbents passivate the surface and prevent the formation of the 2DEG, whereas it can be fully developed at the clean surface. Careful analysis of the Fermi wave vector k_F and of the splitting value between d_{xy} and d_{yz} bands can only confirm that no change in the conduction band is observed within the experimental resolution (around 10 meV) for either the N-A or the A samples upon bending. This finding suggests that the maximum strain generated by our bender ($\approx 0.1\%$) is too small to distinctly alter the conduction band of STO.

Along with the conduction band, the valence band has also been examined. Figures 3(a), 3(d), 3(g), and 3(j) display the valence band, measured along the XΓX high-symmetry direction, of both N-A and a samples, around $\overline{\Gamma}_{00}$ and $\overline{\Gamma}_{10}$. The energy distribution curves (EDCs) in Figs. 3(b), 3(c), 3(e), 3(f), 3(h), 3(i), 3(k), and 3(l) were integrated and indicated by dashed lines in panels (a), (d), (g), and (j).

First, we observe that annealing causes a noticeable spectral weight redistribution from the peak at −5 to the one at −7 eV. Somewhat surprisingly, already at a low applied strain of about 0.1%, the in-gap states undergo noticeable spectroscopic changes, even though the surface conduction band is stable as seen in Fig. 2. While the N-A sample is essentially unaffected, the A sample shows a broadening of the O 2p band and a further increase in the intensity of the peak at −7 eV. Zooming in the in-gap state's region, spanning from the onset of the valence band to E_F (represented by the black rectangles), exposes additional changes. While
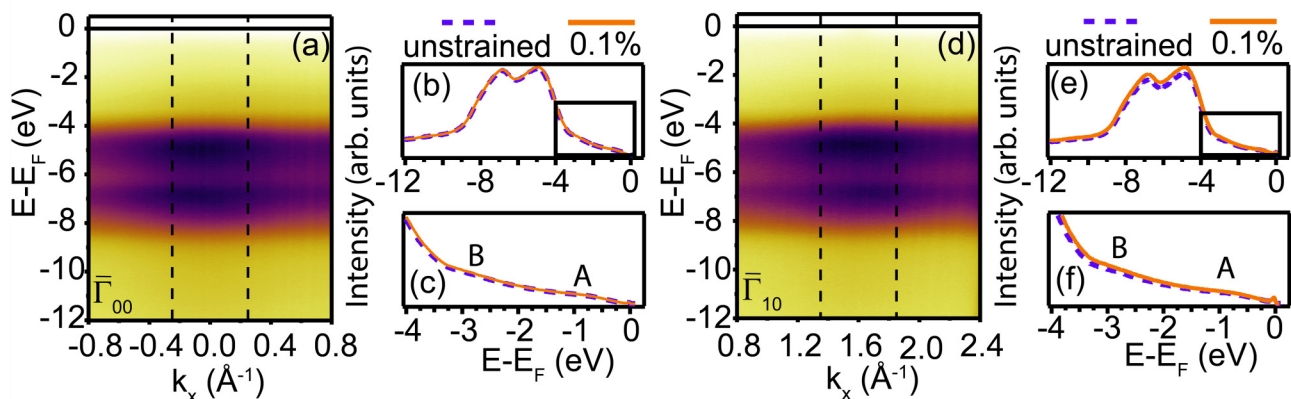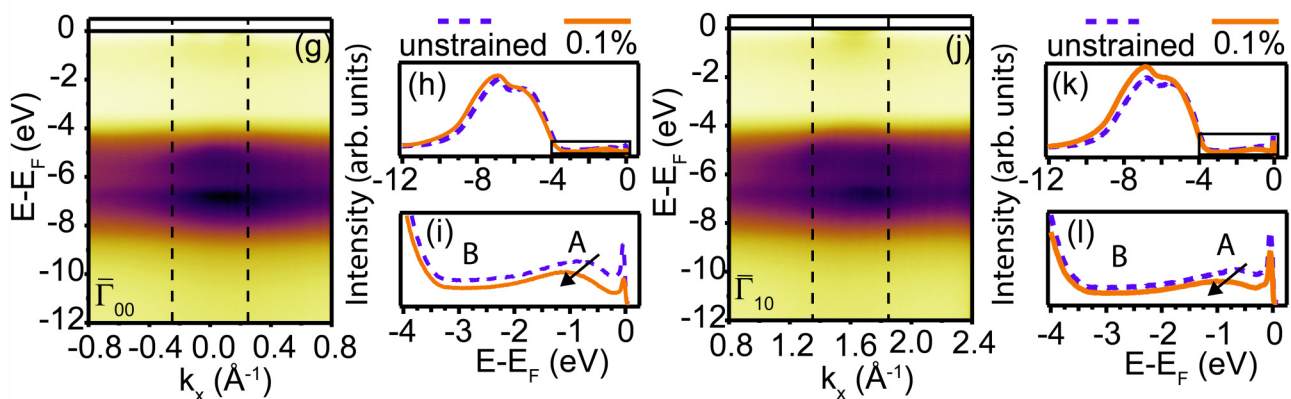
FIG. 3. Valence bands of the 0.1% strained nonannealed (N-A, top row) and the annealed (A, bottom row) samples around the $\overline{\Gamma}_{00}$- (a) and (g) and $\overline{\Gamma}_{01}$-points (d) and (j). The measured valence bands correspond to the cut indicated by the line in the Fermi surfaces presented in Fig. 2 for both strained, N-A, and A samples. The energy distribution cuts (EDCs) in panels (b), (e), (h), and (k) are integrated within the region indicated by dotted lines. Panels (c), (f), (i), and (l) display zoom of the EDC, which enhances the region of in-gap states, which is indicated by the dotted box on the EDCs.

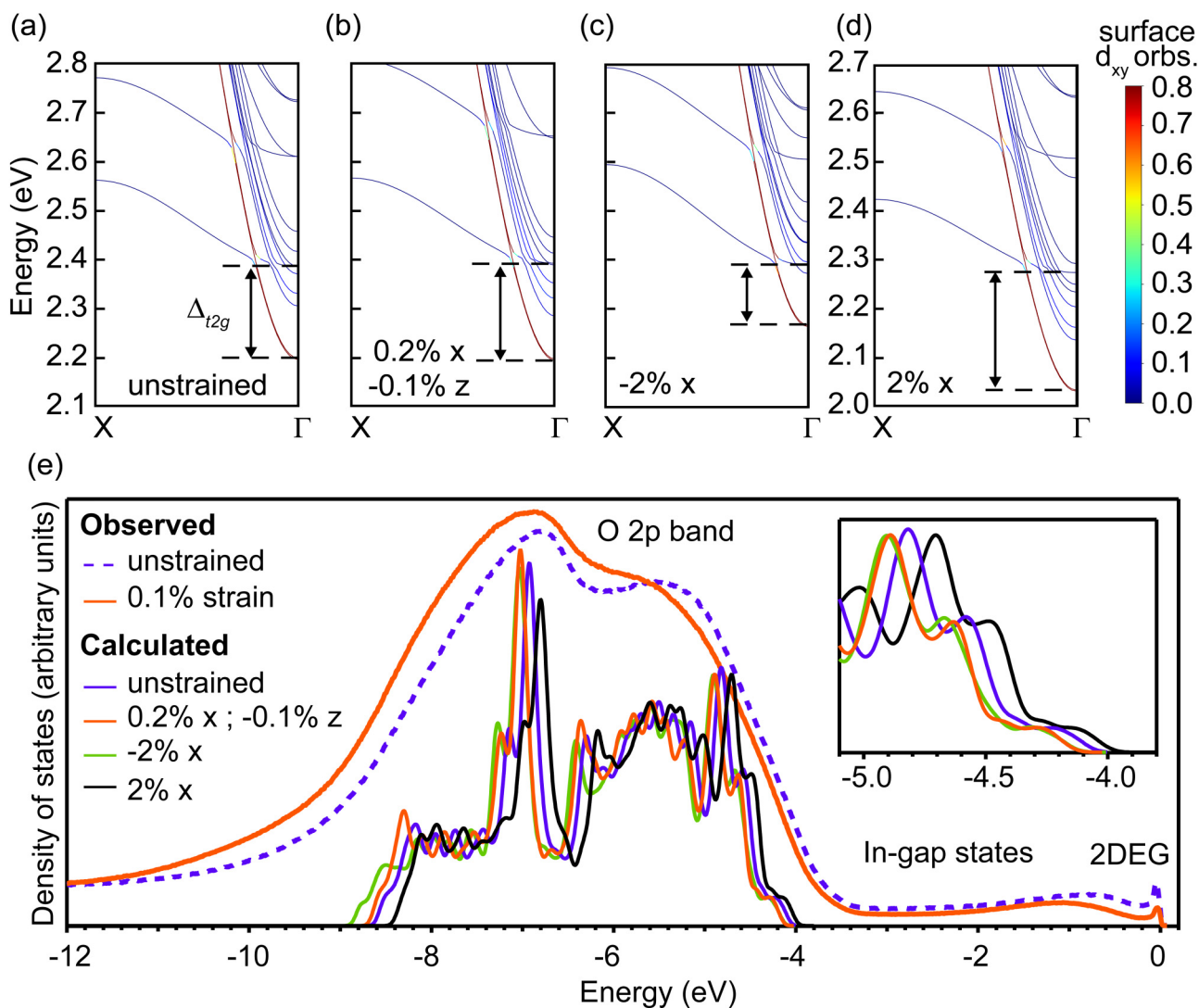**FIG. 4.** Calculated band structures of the STO slab with and without strain. The color map indicates the contribution from Ti-3d_{xy} states of atoms within the TiO$_2$ layer just below the SrO surface termination. (a) 0% strain, (b) 0.2% strain along x and -0.1% strain along z, (c) -2% strain along x, and (d) 2% strain along x. Panel (e) shows a comparison between the measured valence bands and the ones calculated for the same strain configurations as in (a)–(d).

the in-gap state (IGS) of the N-A sample clearly shows two local maxima around 1 and 2.8 eV, the A sample shows spectral weight only around 1 eV. With applied strain, the IGSs shift to higher binding energies and lose intensity.

The IGSs have been associated with the existence of a variety of point defects in the crystal,[32–35] which give rise to localized electronic states such as in doped semiconductors or, more intricately, induce the formation of small polarons, quasiparticles arising due to strong, short-range electron-phonon interaction, which show a typical binding energy of 1 eV.[36–39] Temperature-dependent ARPES data show that the high-binding energy IGS (peak B indicated by arrows around -2.8 eV in the zoom panels) is robust

under the irradiation and temperature cycling during photoemission experiments, while the peak at lower binding energies (peak A indicated by arrows on the zoom panels, around 1 eV) underwent an energy shift and yet vanished with increasing temperature.[18] Because of their distinct temperature evolution, the IGSs A were associated with the formation of small polarons while the IGS B to simple defects. Accordingly, the energy shift and intensity depletion of peak A for strained STO can be attributed to a mutation in the crystal lattice of the surface region, which might influence the interplay between the conduction electrons and the lattice.

In order to conjecture and examine how strain alters the conduction band and controls the electronic properties of the STO

TABLE I. Calculated splitting between d_{xy} and d_{yz} bands (Δ_{t2g}) under different strain configurations.

x (%)	z (%)	Δ_{t2g} (eV)
0	0	0.188
−2	0	0.124
2	0	0.244
0	−2	0.244
0	2	0.138
0.2	−0.1	0.195
2	−2	0.281
2	2	0.179

x (%)	y (%)	Δ_{t2g} (eV)
2	2	0.117
−2	−2	0.248

surface, we performed density functional theory (DFT) simulations of STO slabs under distinct strain configurations defined by $a - a_0/a_0$, where a_0 is the bulk lattice parameter, as shown in Fig. 4. Our previous study reveals that only the SrO-terminated slab band structure is distinguished with the surface state with d_{xy} character, which is significantly lower than d_{xz} and d_{yz} bands.[18] Therefore, we also used the SrO-terminated slab as the model system and focussed on the surface band structure response to various strains. Also, for simplicity, we did not include oxygen vacancies or other possible defects in our calculations. We have calculated the band structure applying different strain values up to 2%, which is reasonable since this value befalls in the range of those found at interfaces between STO and other oxides (LAO, for instance).

The calculations indicate that the energy splitting between the Ti $3d_{xy}$ and Ti $3d_{yz}$ states (Δ_{t2g}) can be efficiently ruled by a complex interplay between applied strain along x- (in-plane) and z-directions (out-of-plane). As shown in Table I and in Fig. 4(a), for no applied strain, a Δ_{t2g} of 188 meV is generated by the intrinsic surface relaxation of a SrO-terminated slab, which is in good agreement with the experimentally observed splitting (see Fig. 2) for the A sample. We denote tensile (compressive) strain with positive (negative) values.

According to the results in Table I, uniaxial tensile strain up to 2% along the x-direction, as shown in Table I and Fig. 4(c), causes Δ_{t2g} to monotonically increase up to 0.244 eV. In turn, for the same values of compressive strain, Δ_{t2g} is monotonically reduced to 0.124 eV [Fig. 4(d)]. The situation is reversed in the case of uniaxial strain along the z-direction, as shown in Table I, for which tensile strain decreases Δ_{t2g} down to 0.138 eV, while compressive strain enhances it up to 0.244 eV. Interestingly, applying 2% in the x-direction has the same effect of applying −2% along the z-direction, which evidences the strong role of intrinsic (out-of-plane) relaxation of the slab surface. Finally, applying tensile strain of 2% in both x- and z- directions leads to a small reduction of Δ_{t2g} to 0.179 eV, while reversing the sign of the strain along the z-direction dramatically increases the splitting to 0.281 eV.

The sample with the maximum applied strain can be represented by the calculation with 0.2% along the x-direction and −0.1% along the z-direction, which shows a slightly increased Δ_{t2g} of 0.195 eV. The conduction band of such a slab is displayed in Fig. 4(b). From the theoretically obtained band structure, a strain level of 0.2% increases the splitting in less than 7 meV, consistent with the results from Fig. 2. Increasing the strain levels to 2% x and −1% results in a Δ_{t2g} of 0.256 eV, while inverting the direction of the strain along z leads to a Δ_{t2g} of 0.201 eV. Finally, we have also calculated structures with applied biaxial in-plane strain, since this configuration is more easily achieved with the growth of heterostructures. A tensile strain of 2% reduces the splitting to 0.117 eV, while the same value of compressive strain increases it to 0.248 eV.

Furthermore, in Fig. 4(e), we study the changes caused by strain in the VB comparing the measured one of the A sample with the calculated density of states (DOS) from the simulations shown in (a)–(d). The calculated valence bands are aligned by their vacuum levels and were rigidly shifted by −4 eV to match the experimental spectra. For simplicity, the calculated conduction band is not shown, since it would appear below the experimental E_F due to the well-known underestimation of the bandgap in calculations using GGA functionals.

The calculated VB is mostly composed of O 2p states. The results reveal that the valence band responds sensibly even to a small strain of 0.2% along the x-direction and −0.1% along the z-direction, overall shifting to higher binding energies. The inset shows the VB leading edge, for which a shift of −0.06 eV is seen. The main panel shows that the peak around −7 eV shifts by −0.09 eV, and the tail of the VB becomes more intense and move by −0.12 eV. These changes with small applied strain are in agreement with the measured VB. For comparison, we also plot the corresponding VB of the structures calculated in Figs. 4(c) and 4(d).

IV. CONCLUSION

By combining the DFT calculation and ARPES, we examined the consequence of the application of strain (uniaxial and biaxial) on the electronic structure of the STO (001) surface. We used a custom-made device to bend and, consequently, generate a strain of around 0.1% on an STO wafer before it cracks. While this level of in-plane tensile strain shows no influence on the electronic structure of the low-dimensional states, it is enough to sensibly alter the in-gap states. Nevertheless, our extensive calculations predict that either compressive or tensile strain levels around 2%, such as the ones achieved with the growth of heterostructures[11] and flexible membranes,[40] induce sizable changes in the 2DEG.

Moreover, by showing that in-gap states are tunable with strain, while band structure modifications require heteroepitaxial growth, our findings offer practical guideposts for engineering the optical properties of STO via the application of strain.

AUTHORS CONTRIBUTIONS

E.B.G. and T.W.J. contributed equally to this work.

DATA AVAILABILITY

The data that support the findings of this study are available from the corresponding author upon reasonable request.

REFERENCES

[1] J. G. Bednorz and K. A. Müller, Z. Phys. B: Condens. Matter **64**, 189 (1986).

[2] R. von Helmolt, J. Wecker, B. Holzapfel, L. Schultz, and K. Samwer, Phys. Rev. Lett. **71**, 2331 (1993).

[3] H. Fujishiro, T. Fukase, and M. Ikebe, J. Phys. Soc. Jpn. **67**, 2582 (1998).

[4] F. J. Morin, Phys. Rev. Lett. **3**, 34 (1959).

[5] B. H. Park, B. S. Kang, S. D. Bu, T. W. Noh, J. Lee, and W. Jo, Nature **401**, 682 (1999).

[6] C. Lu, W. Hu, Y. Tian, and T. Wu, Appl. Phys. Rev. **2**, 021304 (2015).

[7] S. R. Spurgeon, P. V. Sushko, S. A. Chambers, and R. B. Comes, Phys. Rev. Mater. **1**, 063401 (2017).

[8] M. Imada, A. Fujimori, and Y. Tokura, Rev. Mod. Phys. **70**, 1039 (1998).

[9] D. G. Schlom, L.-Q. Chen, C.-B. Eom, K. M. Rabe, S. K. Streiffer, and J.-M. Triscone, Ann. Rev. Mater. Res. **37**, 589 (2007).

[10] B. Burganov et al., Phys. Rev. Lett. **116**, 197003 (2016).

[11] A. Ohtomo and H. Hwang, Nature **427**, 423 (2004).

[12] T. C. Kaspar, P. V. Sushko, S. R. Spurgeon, M. E. Bowden, D. J. Keavney, R. B. Comes, S. Saremi, L. Martin, and S. A. Chambers, Adv. Mater. Interfaces **6**, 1801428 (2019).

[13] A. F. Santander-Syro et al., Nature **469**, 189 (2011).

[14] W. Meevasana, P. D. C. King, R. H. He, S.-K. Mo, M. Hashimoto, A. Tamai, P. Songsiriritthigul, F. Baumberger, and Z.-X. Shen, Nat. Mater. **10**, 114 (2011).

[15] N. C. Plumb et al., Phys. Rev. Lett. **113**, 086801 (2014).

[16] R. Di Capua et al., Phys. Rev. B **86**, 155425 (2012).

[17] P. D. C. King et al., Nat. Commun. **5**, 3414 (2014).

[18] E. B. Guedes, S. Muff, W. H. Brito, M. Caputo, H. Li, N. C. Plumb, J. H. Dil, and M. Radović, Adv. Sci. **8**, 2100602 (2021).

[19] S. N. Rebec, T. Jia, H. M. Sohail, M. Hashimoto, D. Lu, Z.-X. Shen, and R. G. Moore, Proc. Natl. Acad. Sci. U.S.A. **116**, 16687 (2019).

[20] E. B. Guedes, S. Muff, M. Fanciulli, A. P. Weber, M. Caputo, Z. Wang, N. C. Plumb, M. Radović, and J. H. Dil, Phys. Rev. Res. **2**, 033173 (2020).

[21] M. Radović, N. Lampis, F. M. Granozio, P. Perna, Z. Ristic, M. Salluzzo, C. M. Schlepütz, and U. Scotti di Uccio, Appl. Phys. Lett. **94**, 022901 (2009).

[22] B. Jalan, S. J. Allen, G. E. Beltz, P. Moetakef, and S. Stemmer, Appl. Phys. Lett. **98**, 132102 (2011).

[23] S. Riccò et al., Nat. Commun. **9**, 4535 (2018).

[24] "COMSOL multiphysics® v. 5.6.," COMSOL AB, Stockholm, Sweden, 2020.

[25] J. P. Perdew, K. Burke, and M. Ernzerhof, Phys. Rev. Lett. **77**, 3865 (1996).

[26] P. E. Blüchl, Phys. Rev. B **50**, 17953 (1994).

[27] G. Kresse and J. Furthmüller, Comput. Mater. Sci. **6**, 15 (1996).

[28] G. Kresse and J. Furthmüller, Phys. Rev. B **54**, 11169 (1996).

[29] A. I. Liechtenstein, V. I. Anisimov, and J. Zaanen, Phys. Rev. B **52**, R5467 (1995).

[30] A. Damascelli, Z. Hussain, and Z.-X. Shen, Rev. Mod. Phys. **75**, 473 (2003).

[31] A. F. Santander-Syro, F. Fortuna, C. Bareille, T. C. Rödel, G. Landolt, N. C. Plumb, J. Dil, and M. Radović, Nat. Mater. **13**, 1085 (2014).

[32] M. Choi, F. Oba, and I. Tanaka, Phys. Rev. Lett. **103**, 185502 (2009).

[33] Y. S. Kim, J. Kim, S. J. Moon, W. S. Choi, Y. J. Chang, J.-G. Yoon, J. Yu, J.-S. Chung, and T. W. Noh, Appl. Phys. Lett. **94**, 202906 (2009).

[34] S. A. Chambers et al., Phys. Rev. B **97**, 245204 (2018).

[35] A. Al-Zubi, G. Bihlmayer, and S. Blügel, Crystals **9**, 580 (2019).

[36] A. Fujimori, A. Bocquet, K. Morikawa, K. Kobayashi, T. Saitoh, Y. Tokura, I. Hase, and M. Onoda, J. Phys. Chem. Solids **57**, 1379 (1996).

[37] H. O. Jeschke, J. Shen, and R. Valenti, New J. Phys. **17**, 023034 (2015).

[38] A. Janotti, J. B. Varley, M. Choi, and C. G. Van de Walle, Phys. Rev. B **90**, 085202 (2014).

[39] X. Hao, Z. Wang, M. Schmid, U. Diebold, and C. Franchini, Phys. Rev. B **91**, 085204 (2015).

[40] R. Xu et al., Nat. Commun. **11**, 3141 (2020).